ChemPubSoc Europe

DOI: 10.1002/cssc.201902272

CHEMSUSCHEM
Full Papers

Rational Localization of Metal Nanoparticles in Yolk–Shell MOFs for Enhancing Catalytic Performance in Selective Hydrogenation of Cinnamaldehyde

Awu Zhou, Yibo Dou, Jian Zhou, and Jian-Rong Li*[a]

The development of sustainable catalysts to simultaneously improve activity and selectivity remains a challenge. Herein, it is demonstrated that metal nanoparticles (MNPs) can be encapsulated into a yolk–shell metal–organic framework (MOF) with controllable spatial localization to optimize catalytic performance. When the MNPs are located in the void space between the shell and the core of the MOF, the resulting MNPs@MOF composites show both high catalytic activity and selectivity toward the hydrogenation of α,β-unsaturated aldehydes. In particular, the easily recoverable and stable Pt_{void}@MOF(Y) shows an exceptionally high selectivity of 98.2% for cinnamyl alcohol at a high conversion of 97%. The excellent performance can be attributed to easy diffusion of the reactants to access highly exposed MNPs in the MOF support, as well as the improved adsorption of the reactant and desorption of the product due to the appropriate metal–support interaction and rich void space between core and shell.

Supported metal nanoparticle (MNP) catalysts are of interest in heterogeneous catalysis because of their fascinating catalytic behavior, in response to challenges in the fine-chemicals industry.[1] However, the leaching/agglomeration of MNPs that usually occurs results in a diminishment of their catalytic activity over time owing to the weak anchorage on supports. On the other hand, strong immobilization of supported stabilizers around MNPs could prohibit the catalytic activity of surface metal atoms.[2] Recently, encapsulating MNPs in porous materials such as zeolites, activated carbon, and metal–organic frameworks (MOFs) by means of appropriate anchorage has been regarded as a sustainable strategy to improve catalytic activity and facilitate catalyst recovery.[3] Moreover, the porous structures can not only serve as templates for synthesizing monodisperse MNPs, but also provide a well-defined microenvironment that can control the selectivity of catalytic reactions on the encapsulated MNPs and avoid the leaching of MNPs.[4] For example, Jiang and co-workers reported Pt@MIL-125/Au as a high-performance photocatalyst for water splitting.[4h] Tang and co-workers synthesized sandwich MIL-101@Pt@MIL-101 for hydrogenation of α,β-unsaturated aldehydes to unsaturated alcohols.[4i] Astruc and co-workers prepared transition metal NPs/ZIF-8 composites for H_2 generation on hydrolysis of ammonia–borane.[4j]

To date, in porous-material-supported MNPs for heterogeneous catalysis, the MNPs either decorate the outer surface or are completely incorporated within the porous materials.[5] In the former case, the MNPs immobilized on the outer surface have high surface energy and tend to migrate and aggregate into larger particles; this leads to loss of catalytic activity during continuous reactions. In addition, the weak metal–support interaction is also unfavorable for stability and selectivity.[6] In the latter case, the inner porous space can ensure uniform dispersion of incorporated MNPs with high stability and catalytic selectivity.[7] However, the critical bottleneck is the slow diffusion rate when the reactants pass through the long path in the support to access active sites of MNPs. The slow diffusion would result in poor reaction efficiency if the rate-limiting step is diffusion of the reactant to the active sites or diffusion of product out of the catalyst. Clearly, the spatial distribution of MNPs in the porous materials brings about a trade-off between the reaction efficiency and selectivity.[8]

The selective hydrogenation of α,β-unsaturated aldehydes (C=O versus C=C) to produce unsaturated alcohols is an essential step in the preparation of various fine chemicals, but achieving high selectivity to the unsaturated alcohols at high conversion is challenging.[9] The use of heterogeneous catalysts is a potential way to achieve both atom-efficient and environmentally friendly chemical procedures. In this work, cinnamaldehyde (CAL), as a representative α,β-unsaturated aldehyde, was chosen as a model substrate to study the effect of the spatial distribution of Pt NPs in Ni/Zn-MOF on the catalytic performance of the MNPs-MOF composites. A series of catalysts were fabricated by controlling spatial distributions of MNPs in/on the MOF during its homoepitaxial growth (Scheme 1). Catalysts in which MNPs are located in the central area and outer surface of Ni/Zn-MOF spheres are denoted MNPs@MOF(S) and MNPs/MOF(S), respectively, and those with MNPs located in the central area and the void space between the shell and the core of the yolk–shell MOF are denoted $MNPs_{in}$@MOF(Y) and $MNPs_{void}$@MOF(Y), respectively. Interestingly, $MNPs_{void}$@MOF(Y)

---

[a] A. Zhou, Dr. Y. Dou, J. Zhou, Prof. Dr. J.-R. Li
Beijing Key Laboratory for Green Catalysis and Separation and
Department of Chemistry and Chemical Engineering
Beijing University of Technology
Beijing 100124 (P. R. China)
E-mail: jrli@bjut.edu.cn

Supporting Information and the ORCID identification number(s) for the author(s) of this article can be found under: https://doi.org/10.1002/cssc.201902272.

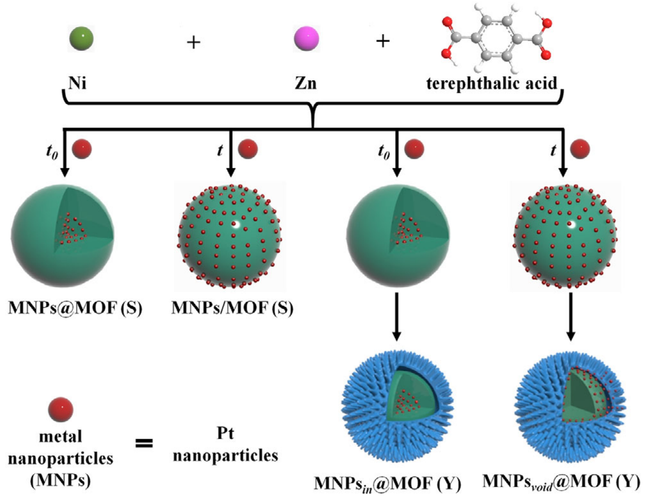

Scheme 1. Schematic illustration of regulating the localization of MNPs in Ni/Zn-MOF microspheres. The spatial distribution of incorporated MNPs in/on the MOF can be controlled by means of the addition subsequence during its homoepitaxial growth: t_0: addition at the beginning, t: after 4.5 h.

shows better catalytic performance than the others. In particular, the easily recoverable and stable Pt_{void}@MOF(Y) shows an exceptionally high selectivity of 98.2% toward cinnamyl alcohol at a high conversion of 97%. The systematic investigation of how the spatial localization of MNPs in the MOF support influences the catalytic performance thus provides a guideline for developing supported catalysts with outstanding performance.

Ni/Zn-MOF-supported Pt NPs were prepared by adjusting the addition sequence of Pt NPs with a size of approximately 5 nm (see Supporting Information, Figure S1) during the growth of the MOF. As shown in Figure 1A, the powder X-ray diffraction (PXRD) patterns of the obtained Pt/MOF(S), Pt@MOF(S), Pt_{in}@MOF(Y), and Pt_{void}@MOF(Y), which show clear characteristic peaks indexed to Ni/Zn-MOF (see the Supporting Information for synthetic details), demonstrate retention of the Ni/Zn-MOF structure after loading with Pt NPs. The absence of diffraction peaks of Pt NPs is probably attributable to the low Pt content in the composites. The formation and associated morphological changes of the Pt/MOF composites were subsequently investigated by SEM and TEM (Figure 1B–D and Figures S2 and S3). Taking Pt_{void}@MOF(Y) as an example, Ni/Zn-MOF(S) microspheres with smooth surface were initially formed after a crystallization time of 1.5 h (Figure 1B). Then, the Pt NPs were added to the solution containing the precursors of Ni/Zn-MOF for crystallization for a further another 4.5 h. Pt_{void}@MOF(Y) with echinoidea-like structure and size of approximately 3 µm was obtained (Figure 1C). The similar structure of pristine Ni/Zn-MOF (Figures S4 and S5) suggests that the encapsulation of Pt NPs did not damage the structure of Ni/Zn-MOF, in agreement with the PXRD result. Importantly, the yolk–shell structure of the MOF and a clear cavity between the outer shell and inner yolk sphere were further revealed by TEM (Figure 1D), in which the Pt NPs with exposed (111) plane are uniformly distributed (Figure S6).[10] Furthermore, the energy-dispersive X-ray spectroscopy (EDS) mapping analysis of Pt_{void}@MOF(Y) showed that the Zn, Ni, and Pt elements in Pt_{void}@MOF(Y) are homogeneously distributed on the Echinoidea-like structure (Figure 1E). Thus, the spatial distribution of incorporated Pt NPs in/on the MOF can be controlled by their addition sequence.[4c, 8a, 9b]

Similarly, the other Pt@MOF composites, Pt@MOF(S) (Figure S2) and Pt_{in}@MOF(Y) (Figure S3), with different morphologies were fabricated by adjusting the addition sequence of Pt NPs. All of the composites show type IV N_2 adsorption isotherms of mesoporous materials with the following order of BET surface areas: MOF ($683\ m^2g^{-1}$) > Pt_{in}@MOF(Y) ($469\ m^2g^{-1}$) > Pt@MOF(S) ($346\ m^2g^{-1}$) > Pt_{void}@MOF(Y) ($297\ m^2g^{-1}$) > Pt/MOF(S) ($180\ m^2g^{-1}$) (Figures S7–S11). These results indicate that some of cavities of the host MOF are probably occupied/blocked by the introduced Pt NPs. In addition, both MOF and Pt@MOF composites showed high H_2 enrichment capability (Figure S12–S16), which is favorable for catalytic hydrogenation.

Then, the effect of the spatial position of MNPs in/on the MOF on the catalytic efficiency and selectivity in the hydrogenation of CAL was investigated (Figure 2A, Table 1). The conversion of CAL on different catalysts as a function of reaction time follows the order of Pt_{void}@MOF(Y) > Pt@MOF(S) > Pt_{in}@MOF(Y) > Pt/MOF(S). Pt/MOF(S) gave only 56% conversion

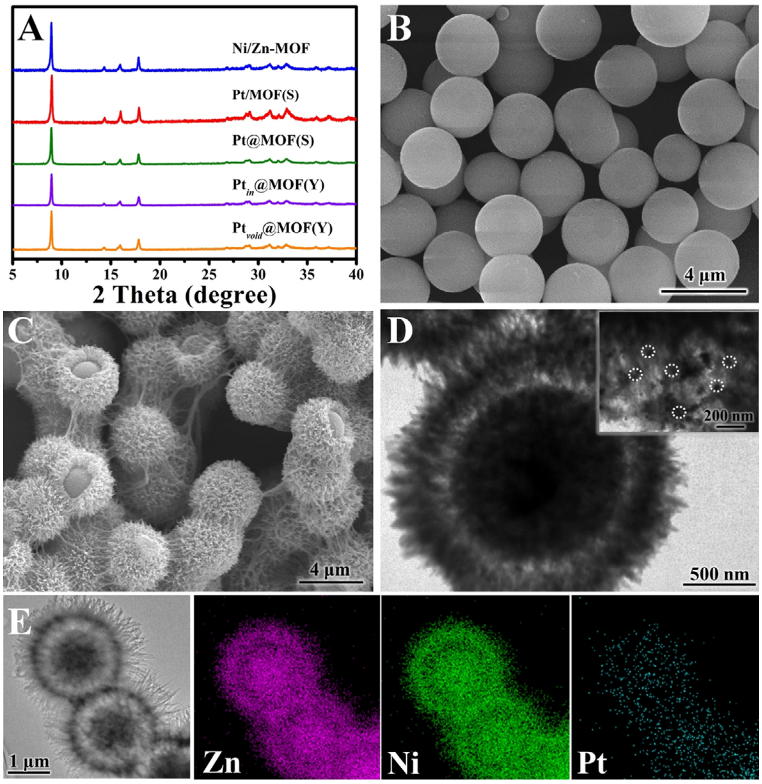

Figure 1. A) PXRD patterns of Ni/Zn-MOF, Pt/MOF(S), Pt@MOF(S), Pt_{in}@MOF(Y), and Pt_{void}@MOF(Y). B) SEM image of Ni/Zn-MOF(S). C) SEM images, D) TEM images (inset: HRTEM image), and E) EDS elemental mapping images of Pt_{void}@MOF(Y).

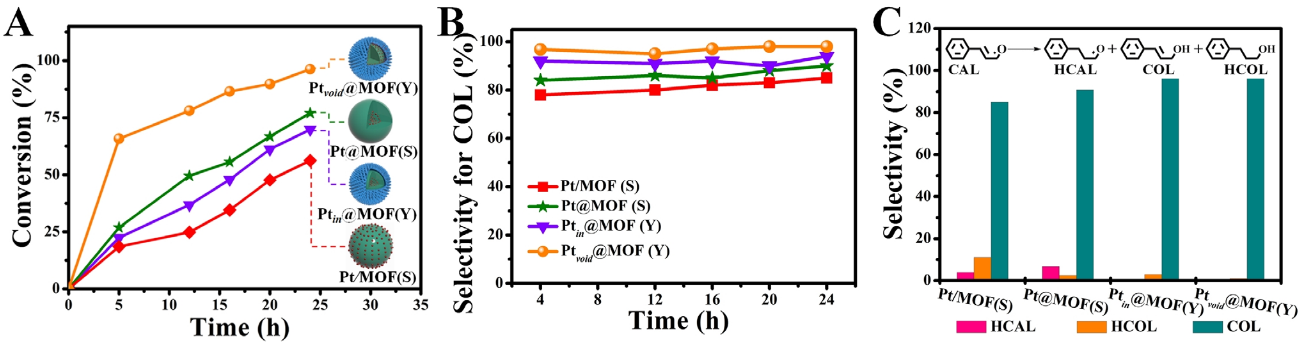

Figure 2. Curves of A) conversion of CAL, B) selectivity for the hydrogenation of CAL to COL as a function of reaction time, and C) selectivity toward HCAL, HCOL, and COL for the hydrogenation of CAL over Pt/MOF(S), Pt@MOF(S), Pt$_{in}$@MOF(Y), and Pt$_{void}$@MOF(Y) for 24 h.

Table 1. Hydrogenation of cinnamaldehyde (CAL) over different catalysts.[a]

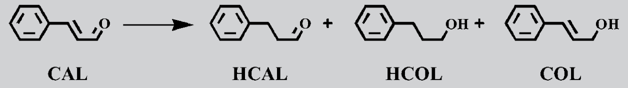

Entry	Catalyst	Time [h]	Conversion[a] [%]	Selectivity[a] [%] HCAL	HCOL	COL	TOF[b] [h^{-1}]
1	Pt/MOF(S)	21.5	50	12.1	9.5	78.4	23.3
2	Pt@MOF(S)	12.3	50	14.7	0	86.3	40.7
3	Pt$_{in}$@MOF(Y)	16.5	50	5.2	2	92.2	30.3
4	Pt$_{void}$@MOF(Y)	3.8	50	1.4	1.8	96.8	131.6
5	Pt/MOF(S)	24	56	3.9	11	85.1	23.4
6	Pt@MOF(S)	24	77	6.7	2.5	90.8	32.1
7	Pt$_{in}$@MOF(Y)	24	70	3.9	1.9	94.2	29.2
8	Pt$_{void}$@MOF(Y)	24	97	0.6	1.2	98.2	40.5

[a] Reaction conditions: CAL (0.5 mmol), catalyst (0.1 mol% Pt NPs), 1 MPa H_2, 50 °C. [b] Percentage conversion of CAL and selectivity for specific products (hydrocinnamaldehyde, HCAL; hydrocinnamyl alcohol, HCOL; cinnamyl alcohol, COL) were determined by GC-MS. [c] TOF = moles of converted COL/(mole of total Pt × reaction time).

of CAL with a turnover frequency (TOF) of 23.4 h^{-1} at 24 h.[11] This low conversion can be explained by the Pt NPs immobilized on the Ni/Zn-MOF surface having high surface energy, which leads to their aggregation and thus to loss of catalytic activity. In contrast, in Pt$_{in}$@MOF(Y) encapsulation of the Pt NPs by the MOF results in increased conversion (70%) and TOF (29.2 h^{-1}) for CAL. This remarkable enhancement is probably due to the specific distribution of Pt active sites. However, the outer thick shell of MOF could inhibit reactant diffusion, as reflected by Pt@MOF(S) with a relatively low conversion of 77% and TOF of 32.1 h^{-1} compared with Pt$_{void}$@MOF(Y). Most importantly, Pt$_{void}$@MOF(Y) exhibits a very high conversion of 97% with a TOF of 40.5 h^{-1}, owing to the shortened diffusion distance of the reactants from the MOF surface to the MNPs active sites. These comparisons thus illustrate that incorporation of the Pt NPs into the MOF can guarantee highly distributed active sites, but also results in a diffusion barrier for reactants accessing active sites through the MOF pores. By modulating the spatial location of Pt NPs in MOF, the Pt active sites located in the void space between core and shell would reduce the diffusion distance of reactants from the MOF surface to MNPs active sites and thus contribute to the greatly enhanced catalytic activity.

The catalytic selectivity of CAL to cinnamyl alcohol (COL) was investigated. Figure 2B shows the selectivity of various catalysts as a function of reaction time. Pt$_{void}$@MOF(Y) exhibited excellent selectivity of 98.2% at 24 h, which is higher than those of Pt/MOF(S) (85.1%), Pt@MOF(S) (90.8%), and Pt$_{in}$@MOF(Y) (94.2%) (Figure 2C). Compared with the bare Pt NPs (64.0%), Pt/LDH (LDH = layered double hydroxide) (24.0%), and Pt/Al_2O_3 (63.4%) (Figure S17, S18, and Table S1), all Pt@MOF composites exhibited improved selectivity toward COL (Table 1, entries 5–8). This could be attributed to the metal–support interaction between Pt and Ni/Zn-MOF, which is beneficial for adsorption and activation of the C=O rather than the C=C bond, and hence higher selectivity toward COL.[12] The MOF can also serve as a selectivity regulator for the hydrogenation of α,β-unsaturated aldehydes.[8a] In particular, the yolk–shell MOF structure can change the chemical environment surrounding the NPs and simultaneously allow reactants access to the active sites. Moreover, steric effects imposed by pores/channels would enhance the selectivity in the case of Pt NPs confined in porous Ni/Zn-MOF. However, Pt/MOF(S) showed only 78.4% selectivity to COL because only the edges of Pt NPs are in direct contact with the Ni/Zn-MOF support. The metal–support interface area is a small fraction of the entire Pt NPs surface, and the exposed metal surface could cause irreversible hydrogenation. On the contrary, the Pt NPs encapsulated within the MOF could create more metal–support interactions. Pt@MOF(S) and Pt$_{in}$@MOF(Y) showed selectivities to COL as high as 86.3 and 92.2%, respectively. The enhanced selectivities most likely result from the steric effect imposed by the MOF shell. The average pore size of Ni/Zn-MOF of approximately 1.3 nm (Figure S19) is very close to the size of CAL (1.05 × 0.65 nm, Figure S20), and this may cause the steric effect. As a result, the narrow channels of the MOF may force the reactant molecules (CAL) to be adsorbed on the encaged Pt particles (≈5 nm, Figure S6) through the C=O bond, and thus access to the C=C bond is restricted. Similar steric effects imposed by pores/channels were proposed to enhance the selectivity in the case of Pt NPs confined in porous materials.[4b] By comparing their conversions, a trade-off phenomenon between improved selectivity and decreased TOF was observed, because the MOF shell not only improves selectivity, but also inhibits the reaction efficiency. Pt_{void}@MOF (Y) exhibited a quite high selectivity of 98.2%. The void space between the MOF shell and core may improve the adsorption of CAL and simultaneously help preferential desorption of COL. In addition, the void space can enhance H_2 adsorption,[13] and the hydrogenation step on the surface of Pt NPs thus favors attack at the $C{=}O$ bond to yield COL.[14] Pt_{void}@MOF(Y) with exceptionally high selectivity and conversion efficiency thus demonstrates the best performance among all reported Pt-based catalysts for CAL hydrogenation (Table S2).

The reusability of Pt_{void}@MOF(Y) was then tested. No obvious degradation of both conversion and selectivity over five successive cycles was observed, and this indicates that the MNPs are well protected by the stable MOF (Figure S21). Moreover, the highly efficient, easily recoverable, and recyclable catalysts can reduce energy costs and waste generation during subsequent workup procedures. The structural integrity was also retained, as verified by PXRD and SEM measurements (Figure S22 and S23). In addition, after removal of the catalyst, the reaction solution did not exhibit any further reactivity under similar conditions, which implies that no catalytically active entities were leached (Figure S24). Evidently, yolk–shell Pt_{void}@MOF(Y) is highly stable against migration and sintering of Pt NPs, and hence exhibits excellent activity, selectivity, and stability for the hydrogenation reaction.

Then, the catalytic mechanism of Pt_{void}@MOF(Y) was studied. As shown in Figure 3 A, the hydrogen temperature-programmed desorption (H_2-TPD) maxima for the catalysts give an order of Pt_{void}@MOF(Y) (348 °C) < Pt@MOF(S) (385 °C) < Pt_{in}@MOF(Y) (390 °C) < Pt/MOF(S) (406 °C). The intensity of desorption peaks increased and the peak positions gradually shifted to lower temperature. These results indicate easier hydrogen dissociation/activation on Pt_{void}@MOF(Y), which facilitates CAL hydrogenation, consistent with the observed relatively high CAL conversion in experiments. Considering that the selectivity and conversion of the Pt-MOF system are higher than those on bare Pt, Pt/LDH, and Pt/Al_2O_3 composites, we speculate that the interaction between Pt and the MOF plays an important role. Hence, X-ray photoelectron spectroscopy (XPS) was performed to analyze the electron transfer in the Pt-MOF composites (Figure 3 B). Compared with those in Pt NPs (74.1 and 70.8 eV for Pt 4$f_{7/2}$ and Pt 4$f_{5/2}$, respectively), the binding energies of Pt@MOF composites show shifts to higher values. On the other hand, a negative shift of the Ni 2$p_{3/2}$ binding energy in the composites compared with that in Ni/Zn-MOF was observed (Figure S25), which reveals the existence of an electronic interaction between the metal and the support.[15] X-ray absorption near-edge structure (XANES) data were also employed to study the local electronic structure of the Pt-based catalyst and the interaction with the Ni/Zn-MOF support (Figure 3 C). It was found that the Pt L_{III}-edge XANES profiles of the Pt/MOF(S) and Pt_{void}@MOF(Y) are similar to that of the Pt foil, but the higher white-line intensity indicates transfer of electrons from the Pt NPs to the Ni/Zn-MOF.

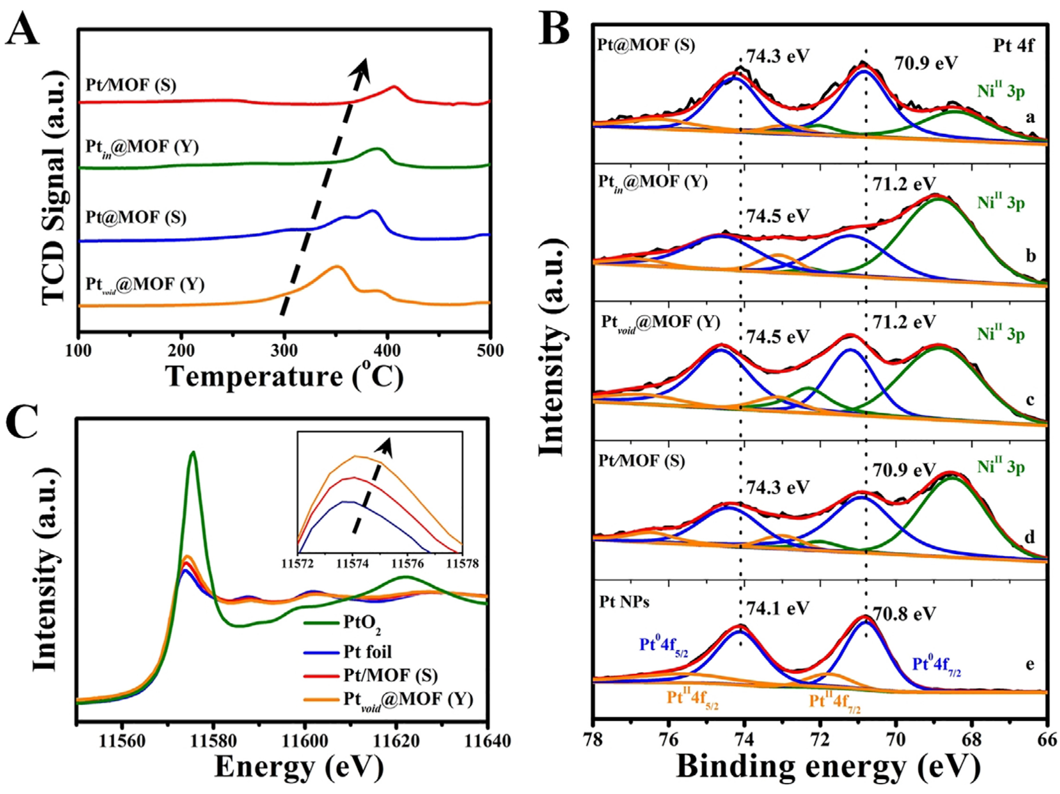

Figure 3. A) H_2 TPD profiles for Pt-MOF composites (TCD: thermal conductivity detector). B) XP spectra in the Pt 4f region of Pt NPs, Pt@MOF composites. C) Normalized XANES spectra at the Pt L_{III}-edge of Pt foil, PtO_2, Pt_{void}@MOF(Y), and Pt/MOF(S); the inset shows a magnified view of a selected region.

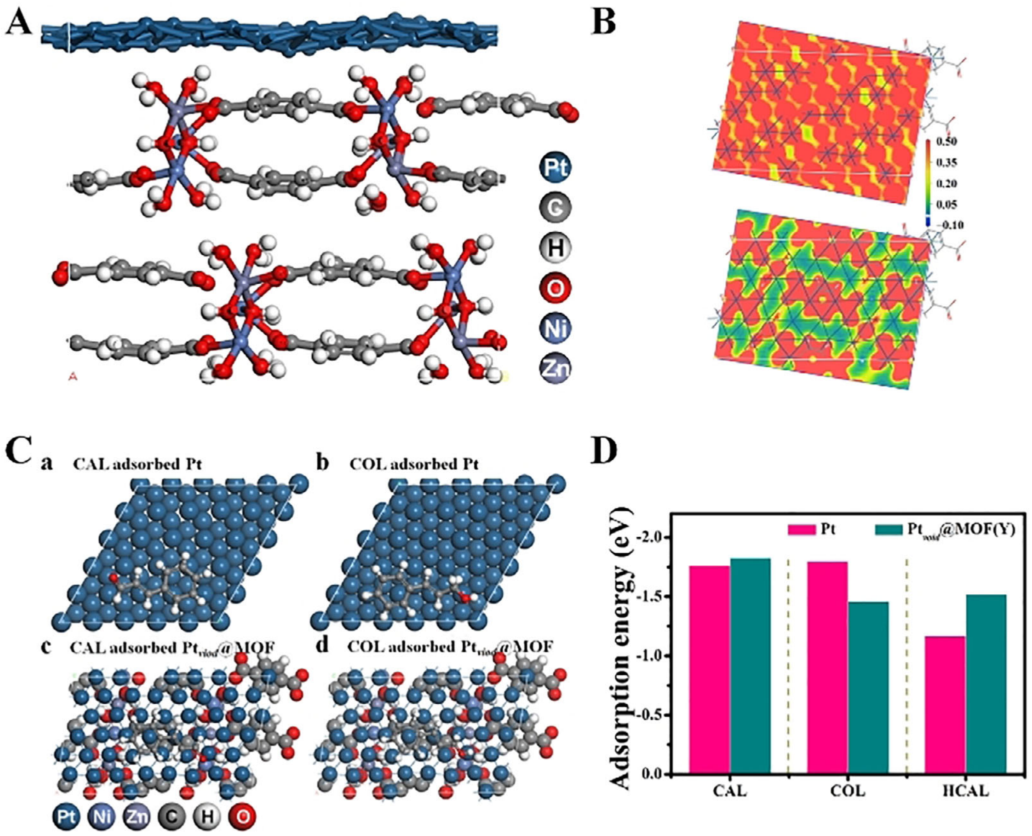

Figure 4. A) Optimized geometric structures of Pt loaded on a Ni/Zn-MOF (111) surface. B) Top views of the electron charge distribution of Pt NPs and MOF on the Pt_{void}@MOF(Y) model. The colored contours show the charge density associated with the defect state ranging from low (blue) to high electron density (red). C) Optimized geometries of a) CAL adsorbed on Pt, b) COL adsorbed on Pt, c) CAL adsorbed on Pt_{void}@MOF(Y), and d) COL adsorbed on Pt_{void}@MOF(Y). D) Adsorption energy [eV] for reactant (CAL) and products (COL and HCAL) in CAL hydrogenation over Pt(111) and Pt_{void}@MOF(Y).

Moreover, the electron charge densities of Pt NPs and Ni/Zn-MOF in a Pt_{void}@MOF(Y) model (Figure 4A) were studied by DFT calculations. The results showed that most of the charge density originates from the Pt (Figure 4B), that is, the lattice-confined Pt atoms contribute favorably to the charge distribution and thus enhance the catalytic activity of the composite. The experimental and theoretical studies thus demonstrate the existence of interfacial electron transfer from Pt to Ni in Ni/Zn-MOF, which may affect the adsorption energy of Pt active sites.[16] Thus, the adsorption structures were explored for CAL, COL, and HCAL over the model Pt(111) and Pt_{void}@MOF(Y) surfaces (Figure 4C), and the adsorption energies are shown in Figure 4D. The calculated adsorption energy of CAL was −1.83 eV on Pt_{void}@MOF(Y), which is clearly higher than that on Pt(111) (−1.76 eV). The stronger adsorption on Pt_{void}@MOF(Y) is thus in favor of increasing the rate of CAL hydrogenation, which is consistent with the experimental results in Table 1. Moreover, it was found that COL is bound more easily to Pt_{void}@MOF (Y) (−1.46 eV) than to Pt(111) (−1.80 eV). The low adsorption energy of COL on the former suggests that the formation of COL is a more facile process over this catalyst.[17] As a result, the easy desorption of COL and the strong adsorption of CAL preferentially favor attack on the C=O bond to yield COL rather than attack at the C=C bond,[18] which is in agreement with the observed increased selectivity toward COL.

Conclusion

We have demonstrated that effective control over the spatial localization of Pt NPs in yolk–shell MOF is very important for simultaneously improving the catalytic efficiency and selectivity of the resulting Pt NPs@MOF catalysts toward the hydrogenation of α,β-unsaturated aldehydes. The catalysts exhibit excellent performance when MNPs are encapsulated in the void space between the MOF core and shell. The yolk–shell structure affords a short diffusion distance of the reactants from the MOF surface to the highly exposed NP active sites. Moreover, the metal–support interaction and the rich void space are favorable for improving the diffusion of molecules, and thus simultaneously contribute to the fast reaction kinetics and high selectivity. This work thus provides a new way to optimize the spatial localization of metal NPs in MOF supports for enhancing catalytic performance, which may be applicable in designing other embedded, supported MNP catalysts.

Experimental Section

Further experimental and computational details are given in the Supporting Information.

Synthesis of yolk–shell Pt_{void}@MOF(Y) microspheres

In a typical procedure, as-synthesized Pt NPs solution (8 mL), H_2BDC (0.06 g), $Ni(NO_3)_2{\cdot}6H_2O$ (0.1 g), and $Zn(NO_3)_2{\cdot}6H_2O$ (0.1 g) were dissolved in a mixture of DMF (16 mL) and ethylene glycol (10 mL) with stirring for 1 h, and then the solution was aged at 150 °C for 1.5 h. As-synthesized Pt NPs solution (8 mL, 0.6 mM) was added dropwise with vigorous stirring for 2 h, and then the mixed solution was further aged at 150 °C for 4.5 h. Subsequently, the precipitate was washed with DMF and alcohol several times and then dried under vacuum at 60 °C overnight. The Pt content (0.15 wt%) of the composites was measured by inductively coupled plasma atomic emission spectroscopy (Varian 710-OES). Pt NPs, yolk–shell Ni/Zn-MOF(Y), Pt/MOF(S), Pt@MOF(S), and yolk–shell Pt_{in}@MOF(Y) microspheres were fabricated (see Supporting Information).

Catalytic selective hydrogenation of cinnamaldehyde (CAL) to cinnamyl alcohol (COL)

Typically, CAL (0.5 mmol) and catalyst (0.1 mol% Pt NPs) were dispersed in isopropyl alcohol (5 mL). After flushing with N_2, the autoclave was purged with H_2 five times, and the final H_2 pressure of the autoclave was set at 1.0 MPa, and it was stirred at 50 °C. Then, the catalysts were separated by centrifugation and washed with ethanol for reuse, and the obtained reaction solution was filtered through a filter membrane (0.22 μM) and then analyzed by GC-MS (Bruker Scion TQ GC-MS/MS equipped with HP-5MS capillary column).

Model construction

The model of Pt was built by using the XRD data (space group $FM\bar{3}M$, with $\alpha=\beta=\gamma=90^\circ$, $a=b=c=3.9239$ Å). The supercell of Pt is 5×5×2 in the *a*, *b*, and *c* directions. Then the (111) facet of Pt was cleaved with a vacuum layer of 15 Å, since the (111) facet has been determined to be the exposed surface by HRTEM. Therefore, the chemical formula of model Pt is Pt_{100}. The model of Ni/Zn-MOF was also built from the XRD data (space group $P\bar{1}$, with $a=10.2077$, $b=8.0135$, $c=6.3337$ Å and $\alpha=97.701$, $\beta=97.213$, $\gamma=108.767^\circ$). The supercell of Ni/Zn MOF is 2×2×1 in the *a*, *b*, and *c* directions. Thus, the chemical formula of model Ni/Zn-MOF is $Ni_6Zn_6C_{64}H_{72}O_{56}$. The model of Pt_{void}@MOF(Y) was constructed by putting one layer of Pt atoms on Ni/Zn-MOF, and the vacuum layer was 15 Å.

Computational Method

All calculations are performed by employing the DFT plane-wave pseudopotential method with the CASTEP code in the Accelrys materials studio version 6.1 software package.[19] The generalized gradient approximation (GGA) Perdew–Burke–Ernzerhof (PBE) functional and the ultrasoft pseudopotentials were used.[20,21] The cutoff energy and Monkhorst–Pack mesh of k points were 380 eV and (6×6×1), respectively. The Broyden–Fletcher–Goldfarb–Shanno (BFGS) algorithm was applied in searching the potential-energy surface during optimization.[22] The structure optimization was based on the following three points: 1) an energy tolerance of 1.0×10^{-5} eVatom^{-1}, 2) a maximum force tolerance of 0.03 eVÅ^{-1}, and 3) a maximum displacement tolerance of 1.0×10^{-3} Å. A Fermi smearing of 0.1 eV and Pulay mixing were employed to guarantee fast convergence of the self-consistent field iterations.[23] The adsorption energy E_{ads} of the adsorbate (CAL or COL) on the surface [Pt or Ptvoid@MOF (Y)] can be calculated with Equation (1):[19,24]

$$E_{ads} = E_{surface+adsorbate} - (E_{surface} + E_{adsorbate}) \quad (1)$$

where $E_{surface}$ is the energy of the investigated surface, $E_{adsorbate}$ the energy of CAL or COL, and $E_{surface+adsorbate}$ the energy of Pt or Pt_{void}@MOF(Y) with CAL or COL adsorbed.

Characterization

PXRD patterns were recorded by using a Rigaku XRD-6000 diffractometer with CuK_α ($\lambda=1.542$ Å) radiation (40 kV, 30 mA). XPS was performed with an ESCA LAB250 spectrometer (Thermo Electron) by using AlK_α radiation. The specific surface area was determined with a Micrometitics Surface Area Analyzer (ASAP 2020). The morphology of the materials was investigated by SEM (Zeiss SUPRA 55) with an accelerating voltage of 20 kV, combined with EDS for elemental analysis. TEM and HRTEM images were were obtained with a JEOL JEM-2100 microscope at an accelerating voltage of 200 kV. The X-ray absorption near-edge structure (XANES) was performed at beamline 1W1B of the Beijing Synchrotron Radiation Facility (BSRF), Institute of High Energy Physics (IHEP), Chinese Academy of Sciences (CAS). The electron beam energy of the storage ring was 2.5 GeV with a stored current of 200 mA.

Acknowledgements

This work was supported by the Natural Science Foundation of China (21576006, 21606006, 51621003). We also thank the National Supercomputing Center in Shenzhen for providing computational resources.

Conflict of interest

The authors declare no conflict of interest.

Keywords: heterogeneous catalysis · hydrogenation · metal–organic frameworks · nanoparticles · supported catalysts

[1] a) M. Behrens, F. Studt, I. Kasatkin, S. Kuehl, M. Haevecker, F. Abild-Pedersen, S. Zander, F. Girgsdies, P. Kurr, B.-L. Kniep, M. Tovar, R. W. Fischer, J. K. Norskov, R. Schloegl, *Science* **2012**, *336*, 893–897; b) S. Li, Y. Xu, Y. Chen, W. Li, L. Lin, M. Li, Y. Deng, X. Wang, B. Ge, C. Yang, S. Yao, J. Xie, Y. Li, X. Liu, D. Ma, *Angew. Chem. Int. Ed.* **2017**, *56*, 10761–10765; *Angew. Chem.* **2017**, *129*, 10901–10905; c) R. Schlögl, *Angew. Chem. Int. Ed.* **2015**, *54*, 3465–3520; *Angew. Chem.* **2015**, *127*, 3531–3589; d) A. Zhou, R.-M. Guo, J. Zhou, Y. Dou, Y. Chen, J.-R. Li, *ACS Sustainable Chem. Eng.* **2018**, *6*, 2103–2111; e) J. M. Campelo, D. Luna, R. Luque, J. M. Marinas, A. A. Romero, *ChemSusChem* **2009**, *2*, 18–45.

[2] a) L. Jiao, Y. Wang, H.-L. Jiang, Q. Xu, *Adv. Mater.* **2018**, *30*, 1703663; b) B. Wu, H. Huang, J. Yang, N. Zheng, G. Fu, *Angew. Chem. Int. Ed.* **2012**, *51*, 3440–3443; *Angew. Chem.* **2012**, *124*, 3496–3499; c) J. Hermannsdörfer, M. Friedrich, N. Miyajima, R. Q. Albuquerque, S. Kummel, R. Kempe, *Angew. Chem. Int. Ed.* **2012**, *51*, 11473–11477; *Angew. Chem.* **2012**, *124*, 11640–11644.

[3] a) M. Yang, S. Li, Y. Wang, J. A. Herron, Y. Xu, L. F. Allard, S. Lee, J. Huang, M. Mavrikakis, M. Flytzani-Stephanopoulos, *Science* **2014**, *346*, 1498–1501; b) G.-H. Wang, J. Hilgert, F. H. Richter, F. Wang, H.-J. Bongard, B. Spliethoff, C. Weidenthaler, F. Schueth, *Nat. Mater.* **2014**, *13*, 294–300; c) G. Li, S. Zhao, Y. Zhang, Z. Tang, *Adv. Mater.* **2018**, *30*, 1800702; d) Y. Dou, J. Zhou, A. Zhou, J.-R. Li, Z. Nie, *J. Mater. Chem. A* **2017**, *5*, 19491–

19498; e) M. Oubenali, G. Vanucci, B. Machado, M. Kacimi, M. Ziyad, J. Faria, A. Raspolli-Galetti, P. Serp, *ChemSusChem* **2011**, *4*, 950–956.

[4] a) Q. Yang, Q. Xu, H.-L. Jiang, *Chem. Soc. Rev.* **2017**, *46*, 4774–4808; b) Z. Guo, C. Xiao, R. V. Maligal-Ganesh, L. Zhou, T. W. Goh, X. Li, D. Tesfagaber, A. Thiel, W. Huang, *ACS Catal.* **2014**, *4*, 1340–1348; c) G. Lu, S. Li, Z. Guo, O. K. Farha, B. G. Hauser, X. Qi, Y. Wang, X. Wang, S. Han, X. Liu, J. S. DuChene, H. Zhang, Q. Zhang, X. Chen, J. Ma, S. C. Loo, W. D. Wei, Y. Yang, J. T. Hupp, F. Huo, *Nat. Chem.* **2012**, *4*, 310–316; d) B. Aguila, Q. Sun, X. Wang, E. O'Rourke, A. M. Al-Enizi, A. Nafady, S. Ma, *Angew. Chem. Int. Ed.* **2018**, *57*, 10107–10111; *Angew. Chem.* **2018**, *130*, 10264–10268; e) V. Pascanu, P. R. Hansen, A. B. Gomez, C. Ayats, A. E. Platero-Prats, M. J. Johansson, M. A. Pericas, B. Martin-Matute, *ChemSusChem* **2015**, *8*, 123–130; f) Y.-Z. Chen, B. Gu, T. Uchida, J. Liu, X. Liu, B.-J. Ye, Q. Xu, H.-L. Jiang, *Nat. Commun.* **2019**, *10*, 3462; g) J. D. Xiao, Q. Shang, Y. Xiong, Q. Zhang, Y. Luo, S. H. Yu, H.-L. Jiang, *Angew. Chem. Int. Ed.* **2016**, *55*, 9389–9393; *Angew. Chem.* **2016**, *128*, 9535–9539; h) J. D. Xiao, L. Han, J. Luo, S. H. Yu, H.-L. Jiang, *Angew. Chem. Int. Ed.* **2018**, *57*, 1103–1107; *Angew. Chem.* **2018**, *130*, 1115–1119; i) M. Zhao, K. Yuan, Y. Wang, G. Li, J. Guo, L. Gu, W. Hu, H. Zhao, Z. Tang, *Nature* **2016**, *539*, 76–80; j) C. Wang, J. Tuninetti, Z. Wang, C. Zhang, R. Ciganda, L. Salmon, S. Moya, J. Ruiz, D. Astruc, *J. Am. Chem. Soc.* **2017**, *139*, 11610–11615.

[5] a) H. Liu, L. Chang, C. Bai, L. Chen, R. Luque, Y. Li, *Angew. Chem. Int. Ed.* **2016**, *55*, 5019–5023; *Angew. Chem.* **2016**, *128*, 5103–5107; b) X.-Y. Liu, F. Zhang, T.-W. Goh, Y. Li, Y.-C. Shao, L. Luo, W. Huang, Y.-T. Long, L.-Y. Chou, C.-K. Tsung, *Angew. Chem. Int. Ed.* **2018**, *57*, 2110–2114; *Angew. Chem.* **2018**, *130*, 2132–2136.

[6] a) S. J. Tauster, *Acc. Chem. Res.* **2002**, *20*, 389–394; b) B. An, J. Zhang, K. Cheng, P. Ji, C. Wang, W. Lin, *J. Am. Chem. Soc.* **2017**, *139*, 3834–3840; c) H. Tang, Y. Su, B. Zhang, A. F. Lee, M. A. Isaacs, K. Wilson, L. Li, Y. Ren, J. Huang, M. Haruta, B. Qiao, X. Liu, C. Jin, D. Su, J. Wang, T. Zhang, *Sci. Adv.* **2017**, *3*, 1700231.

[7] M. Zhao, K. Deng, L. He, Y. Liu, G. Li, H. Zhao, Z. Tang, *J. Am. Chem. Soc.* **2014**, *136*, 1738–1741.

[8] a) K. Yuan, T. Song, D. Wang, X. Zhang, X. Gao, Y. Zou, H. Dong, Z. Tang, W. Hu, *Angew. Chem. Int. Ed.* **2018**, *57*, 5708–5713; *Angew. Chem.* **2018**, *130*, 5810–5815; b) Q. Yang, W. Liu, B. Wang, W. Zhang, X. Zeng, C. Zhang, Y. Qin, X. Sun, T. Wu, J. Liu, F. Huo, J. Lu, *Nat. Commun.* **2017**, *8*, 14429; c) C.-H. Kuo, Y. Tang, L.-Y. Chou, B. T. Sneed, C. N. Brodsky, Z. Zhao, C.-K. Tsung, *J. Am. Chem. Soc.* **2012**, *134*, 14345–14348.

[9] a) H. Liu, L. Chang, L. Chen, Y. Li, *ChemCatChem* **2016**, *8*, 946–951; b) E. Plessers, D. E. De Vos, M. B. J. Roeffaers, *J. Catal.* **2016**, *340*, 136–143.

[10] X.-Q. Wu, J. Zhao, Y.-P. Wu, W.-w. Dong, D.-S. Li, J.-R. Li, Q. Zhang, *ACS Appl. Mater. Interfaces* **2018**, *10*, 12740–12749.

[11] D. Yang, H. Yu, T. He, S. Zuo, X. Liu, H. Yang, B. Ni, H. Li, L. Gu, D. Wang, X. Wang, *Nat. Commun.* **2019**, *10*, 3844.

[12] a) M. G. Prakash, R. Mahalakshmy, K. R. Krishnamurthy, B. Viswanathan, *Catal. Today* **2016**, *263*, 105–111; b) H. Wang, S. Bai, Y. Pi, Q. Shao, Y. Tan, X. Huang, *ACS Catal.* **2019**, *9*, 154–159.

[13] Q. Yue, J. Li, Y. Zhang, X. Cheng, X. Chen, P. Pan, J. Su, A. A. Elzatahry, A. Alghamdi, Y. Deng, D. Zhao, *J. Am. Chem. Soc.* **2017**, *139*, 15486–15493.

[14] H. Pan, J. Li, J. Lu, G. Wang, W. Xie, P. Wu, X. Li, *J. Catal.* **2017**, *354*, 24–36.

[15] a) M. Xu, S. He, H. Chen, G. Cui, L. Zheng, B. Wang, M. Wei, *ACS Catal.* **2017**, *7*, 7600–7609; b) B. An, K. Cheng, C. Wang, Y. Wang, W. Lin, *ACS Catal.* **2016**, *6*, 3610–3618.

[16] a) D. Blackmond, *J. Catal.* **1991**, *131*, 401–411; b) D. Loffreda, F. Delbecq, F. Vigné, P. Sautet, *Angew. Chem. Int. Ed.* **2005**, *44*, 5279–5282; *Angew. Chem.* **2005**, *117*, 5413–5416.

[17] M. S. Ide, B. Hao, M. Neurock, R. J. Davis, *ACS Catal.* **2012**, *2*, 671–683.

[18] S. Laref, F. Delbecq, D. Loffreda, *J. Catal.* **2009**, *265*, 35–42.

[19] S. J. Clark, M. D. Segall, C. J. Pickard, P. J. Hasnip, M. J. Probert, K. Refson, M. C. Payne, *Z. Kristallogr. - Cryst. Mater.* **2005**, *220*, 567–570.

[20] J. Perdew, K. Burke, M. Ernzerhof, *Phys. Rev. Lett.* **1996**, *77*, 3865–3868.

[21] D. Vanderbilt, *Phys. Rev. B* **1990**, *41*, 7892–7895.

[22] J. M. Anglada, J. M. Bofill, *J. Comput. Chem.* **1998**, *19*, 349–362.

[23] Á. Valdés, Z. W. Qu, G.-J. Kroes, J. Rossmeisl, J. K. Nørskov, *J. Phys. Chem. C* **2008**, *112*, 9872–9879.

[24] M. Lessio, E. A. Carter, *J. Am. Chem. Soc.* **2015**, *137*, 13248–13251.

Manuscript received: August 21, 2019
Revised manuscript received: September 25, 2019
Accepted manuscript online: September 26, 2019
Version of record online: ■■ ■■, 0000

*A. Zhou, Y. Dou, J. Zhou, J.-R. Li**

■■–■■

Rational Localization of Metal Nanoparticles in Yolk–Shell MOFs for Enhancing Catalytic Performance in Selective Hydrogenation of Cinnamaldehyde

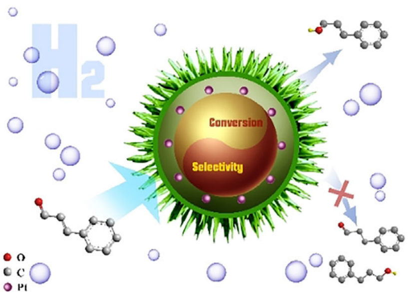

Spatial control: Controlling the spatial localization of metal nanoparticles (MNPs) in yolk–shell MOFs can improve catalytic efficiency and selectivity in the hydrogenation of α,β-unsaturated aldehydes. Catalysts in which the MNPs are encapsulated in the void space between the MOF core and shell exhibit excellent performance due to the favorable metal–support interaction and rich void space between core and shell.